Physics-Based Analytical Channel Charge Model of $In_xGa_{1-x}As/In_{0.52}Al_{0.48}As$ Quantum-Well Field-Effect Transistors From Subthreshold to Strong Inversion Regimes

HYEON-SEOK JEONG[1] (Graduate Student Member, IEEE),
WAN-SOO PARK[1] (Graduate Student Member, IEEE), **HYEON-BHIN JO**[1],
IN-GEUN LEE[1] (Member, IEEE), **TAE-WOO KIM**[2], **TAKUYA TSUTSUMI**[3] (Member, IEEE),
HIROKI SUGIYAMA[3], **HIDEAKI MATSUZAKI**[3] (Senior Member, IEEE), **SUNG-HO HAHM**[1],
JAE-HAK LEE[1], AND **DAE-HYUN KIM**[1] (Member, IEEE)

1 School of Electronic and Electrical Engineering, Kyungpook National University, Daegu 41566, South Korea
2 Electrical Engineering Department, University of Ulsan, Ulsan 41610, South Korea
3 NTT Device Technology Laboratories, Kanagawa 243-0198, Japan

CORRESPONDING AUTHOR: D.-H. KIM (e-mail: dae-hyun.kim@ee.knu.ac.kr)

ABSTRACT This paper presents a physics-based analytical channel charge model for indium-rich $In_xGa_{1-x}As/In_{0.52}Al_{0.48}As$ quantum-well (QW) field-effect transistors (FETs) that is applicable from the subthreshold to strong inversion regimes. The model requires only seven physical/geometrical parameters, along with three transition coefficients. In the subthreshold regime, the conduction bands (E_C) of all regions are flat with finite and symmetrical QW configurations. Since the Fermi–level (E_F) is located far below E_C, the two-dimensional electron-gas density (n_{2-DEG}) should be minimal and can thus be approximated from Maxwell–Boltzmann statistics. In contrast, the applied gate bias lowers the E_C of all structures in the inversion regime, yielding band-bending of an $In_{0.52}Al_{0.48}As$ insulator and $In_xGa_{1-x}As$ QW channel. The dependency of the energy separation between E_F and E_C on the surface of the $In_xGa_{1-x}As$ QW channel upon V_{GS} enables construction of the charge–voltage behaviors of $In_xGa_{1-x}As/In_{0.52}Al_{0.48}As$ QW FETs. To develop a unified, continuous and differentiable areal channel charge density (Q_{ch}) model that is valid from the subthreshold to strong inversion regimes, the previously proposed inversion-layer transition function is further revised with three transition coefficients of η, α and β in this work. To verify the proposed approach, the results of the proposed model are compared with those of not only the numerically calculated Qch from a one-dimensional (1D) Poisson–Schrödinger solver, but also the measured gate capacitance of a fabricated $In_{0.7}Ga_{0.3}As$ QW metal-insulator-semiconductor FET with large gate length, yielding excellent agreement between the simulated and measured results.

INDEX TERMS $In_xGa_{1-x}As/In_{0.52}Al_{0.48}As$ QW FETs, two-dimensional electron-gate density (n_{2-DEG}), subthreshold regime, inversion regime, near-threshold regime.

I. INTRODUCTION

Indium-rich $In_xGa_{1-x}As/In_{0.52}Al_{0.48}As$ quantum-well (QW) field-effect transistors (FETs) on InP substrates are being increasingly used in ultra–high–frequency and low–noise circuit applications. The superior electron ballistic mobility and virtual-source injection velocity of $In_xGa_{1-x}As/In_{0.52}Al_{0.48}As$ material systems are the key determinants of their use as active components in

various integrated circuits, including low-noise amplifiers (LNAs) [1]–[5]. Moreover, these devices have been extensively used in high-frequency applications such as microwave and millimeter-wave analog, mixed-signal, and high-speed telecommunication systems, and are critical especially in future 6G applications [6]–[9]. Designing circuits to operate in such regimes requires accurate and charge–conservative compact models for the areal channel charge density (Q_{ch}) such that they are grounded in device physics and material fundamentals. Besides, these models should be capable of describing the temperature dependence of Q_{ch}, especially at low temperatures of 4 K since high–electron–mobility transistor (HEMT)-based LNAs are extensively utilized as the first stage for detecting noisy quantum-bit signals of quantum computing systems in cryogenic environments [10]–[11].

The pioneering work by Delagebeaudeuf and Linh in 1982 [12], who proposed simplified analytical expressions for the areal channel charge density (Q_{ch}) in $Al_xGa_{1-x}As/GaAs$ material systems for the first time, is still being used as a cornerstone approach in numerous compact models for many III-V devices, including $Al_xGa_{1-x}As/In_yGa_{1-y}As$ pseudomorphic HEMTs on GaAs, $In_xGa_{1-x}As/In_{0.52}Al_{0.48}As$ HEMTs on InP and $Al_xGa_{1-x}N/GaN$ HEMTs on SiC substrates. Historically, most Qch models of Section III-V devices were formulated to cater to microwave applications. Hence, many of these models are either table based or empirical, relying on several fitting parameters for accuracy improvement. However, this inherently reduces their predictive capabilities from one technology generation to the next and from one environmental temperature to the other, as such models lack physics–based formulations of the device operations in various regimes.

Three different types of channel charge models have been utilized so far: the MIT virtual-source (MVS) HEMT model; surface–potential–based HEMT model; and traditional empirical HEMT models, such as Angelov and EE-HEMT [13]–[16]. The MVS model was originally developed for highly scaled Si CMOS devices with near-ballistic transport and has been extended for use in $In_xGa_{1-x}As/In_{0.52}Al_{0.48}As$ and GaN HEMTs with modifications to some of the model parameters [13], [17]–[19]. The surface-potential model relies on self-consistent calculations of the surface potential derived from the semiempirical approximation of band occupation [14], [20]. The Angelov model, which was first proposed by Iltcho Angelov of Chalmers University in 1992 [15], uses the tanh formulation to ensure that both current and charge expressions are continuous in all regimes and have infinitely many derivatives, thereby enabling simulation of large-signal behaviors in such devices. Recently, the Angelov model has been successfully extended to GaN HEMTs [21] and $In_xGa_{1-x}As/In_{0.52}Al_{0.48}As$ HEMTs [22]. The EE HEMT model, which was originally proposed for GaAs HEMTs as an extension of the Curtice model [23], is an empirical model developed by Agilent Technologies for the purpose
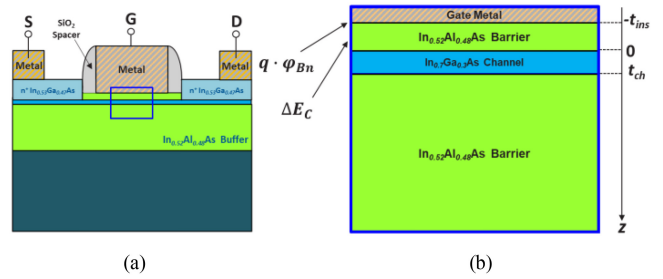

FIGURE 1. (a) Cross-sectional schematic of $In_xGa_{1-x}As/In_{0.52}Al_{0.48}As$ QW MISFET [25] and (b) magnified sketch of the pill-box.

of fitting the measured electrical characteristics of HEMTs with many fitting parameters [16], [24]. However, most of the above models do not consider the materials' fundamentals and physics, limiting their usage from one technology generation to the next and from one temperature to another.

In this work, we present a fully physics–based analytical channel charge model for indium-rich $In_xGa_{1-x}As/In_{0.52}Al_{0.48}As$ QW FETs that is applicable from the subthreshold to strong inversion regimes. The proposed model requires seven physical and geometrical parameters: the Schottky barrier height ($q \cdot \varphi_{BN}$), conduction–band discontinuity (ΔE_C), channel–layer thickness (t_{ch}), insulator layer thickness (t_{ins}), permittivity of the channel layer (ε_{r_ch}), permittivity of the insulator layer (ε_{r_ins}) and in-plane effective mass ($m_{||}^*$) of the channel layer. The model also considers the density of states (DOS) bottleneck and quantum–mechanical (QM) effects through two parameters (a and b), while three transition coefficients (η, α and β) are incorporated to continuously combine the subthreshold and inversion regimes. We applied the proposed analytical model to accurately predict the channel charge density of an $In_{0.7}Ga_{0.3}As/In_{0.52}Al_{0.48}As$ QW metal–insulator–semiconductor FET, which yielded excellent agreement with the measured data.

II. THEORY

Figure 1 (a) illustrates a cross-sectional schematic of the indium-rich $In_xGa_{1-x}As/In_{0.52}Al_{0.48}As$ QW MISFET with source/drain regrown contacts [25]. The coordinate system is selected to point toward the wafer, with the origin placed at the $In_xGa_{1-x}As/In_{0.52}Al_{0.48}As$ heterointerface, from top to bottom. Application of the Gauss law to this situation is straightforward. If we construct a "pill box" that includes all the semiconductor charge densities and penetrates the gate metal partially, as shown in Fig. 1 (b), this is equivalent to a one-dimensional (1D) case. Figure 2 shows two types of energy band diagrams in the z direction of Fig. 1(b). Depending on the difference between $q \cdot \varphi_{BN}$ and ΔE_C, there exist two types of device operation: the first is the normally–off operation (enhancement–mode) for $q \cdot \varphi_{BN} > \Delta E_C$ (Fig. 2 (a)) and the other is the normally–on operation (depletion–mode) for $q \cdot \varphi_{BN} > \Delta E_C$ (Fig. 2 (b)).

FIGURE 2. Conduction band energy diagram of an $In_xGa_{1-x}As/In_{0.52}Al_{0.48}As$ QW FET: (a) normally-off operation and (b) normally-on operation.

Let us then define the applied gate–to–source voltage (V_{GS}) as the threshold voltage (V_T) such that the Fermi–level (E_F) touches the bottom of the conduction band in the QW channel on the surface of $In_xGa_{1-x}As$. This yields a formula for V_T as follows:

$$V_T = \varphi_{Bn} - \Delta E_c/q \tag{1}$$

The threshold condition is also plotted in Figs. 2 (a) and (b). Since nearly the majority of reported devices with $In_xGa_{1-x}As/In_{0.52}Al_{0.48}As$ material systems exhibited normally–on operation [26]–[29], we will address the 1D electrostatics of Fig. 2 (b) in the remainder of this work. In the following sub–sections, we will first examine the charge–voltage behaviors in the subthreshold and inversion regimes separately. Then, we will discuss an approach to continuously combine these two regimes using the widely used inversion-layer transition function.

(a) Subthreshold regime: Let us first derive an analytical expression for the areal channel charge density (Q_{ch}) in the subthreshold regime ($V_{GS} < V_T$). As shown in Fig. 3 (a), Ec of all the region is flat in the subthreshold case, where the $In_xGa_{1-x}As$ channel layer has a symmetrical and rectangular QW configuration with a finite well height of ΔE_C. Since the $In_xGa_{1-x}As$ channel layer is a direct bandgap semiconductor material where the Γ–valley, which is the minimum energy valley of the conduction band, is spherical with respect to the momentum, the DOS function for a two-dimensional sample is given as in Fig. 3 (b). An important consequence of the two-dimensional (2D) DOS is that it is independent of energy as shown in Fig. 3 (b). Thus, only the in-plane effective mass ($m_{\parallel}^*$) determines the 2D DOS of each subband and the electron transport property in the QW plane, whereas the perpendicular effective mass (m^*) sets the location of each subband energy level (E_i). If the QW plane is in the direction of the x-y plane, $m_{\parallel}^*$ and m^* are equal to $\sqrt{m_x^* m_y^*}$ and m_z^*, respectively. In terms of mathematical expressions, the DOS function for $In_xGa_{1-x}As$, $g(E)$, is given as follows (by considering only the three lowest subbands):

$$
\begin{aligned}
g(E) &= 0 &&\text{for } E \leq E_0 \\
&\quad D &&\text{for } E_0 \leq E \leq E_1 \\
&\quad 2 \times D &&\text{for } E_1 \leq E \leq E_2 \\
&\quad 3 \times D &&\text{for } E_2 \leq E
\end{aligned}
\tag{2}
$$

(a)

(b)

FIGURE 3. E_C of the $In_xGa_{1-x}As/In_{0.52}Al_{0.48}As$ QW FET in the subthreshold regime and (b) the density of states function, $g(E)$, for the 2D system.

Here, the constant D is defined as

$$D = \frac{m_{\parallel}^*}{\pi \hbar^2} \tag{3}$$

Armed with the *Fermi–Dirac* statistics, $f(E)$, and $g(E)$ above, the two–dimensional electron gas density, $n_{2\text{-}DEG}$, in units of cm^{-2}, is computed by integrating the electron energy distribution across the entire conduction band. This is mathematically expressed as

$$n_{2\text{-}DEG} = \int_{E_c}^{\infty} f(E) \cdot g(E) dE \tag{4}$$

If we substitute Eq. (2) into Eq. (4), we obtain

$$
n_{2\text{-}DEG} = \int_{E_0}^{E_1} f(E) \cdot D \, dE + \int_{E_1}^{E_2} f(E) \cdot 2D \, dE \\
+ \int_{E_2}^{\infty} f(E) \cdot 3D \, dE \tag{5}
$$

Since E_C is far from E_F in the subthreshold regime, we can simply use the *Maxwell–Boltzmann* statistics. Moreover, it is sufficient to consider the electron population only at the 1st lowest subband. Together, this yields

$$n_{2\text{-}DEG} \approx \frac{m_{\parallel}^*}{\pi \hbar^2} \cdot kT$$

$$\cdot exp\left[\frac{q}{kT}\cdot\left(\frac{\Delta E_c}{q}-\varphi_{Bn}-\frac{h^2}{q\cdot 8m_{||}^*\left[t_{ch}+\frac{2}{\sqrt{2\cdot\Delta E_c}}\right]^2}\right)\right]$$
$$\cdot exp\frac{q\cdot V_{GS}}{kT} \tag{6}$$

As expected, $n_{2\text{-}DEG}$ in the subthreshold regime changes with V_{GS} in an exponential manner and can be determined from four parameters, namely $m_{||}^*$, ΔE_C, φ_{Bn} and t_{ch}. We can then rewrite the above expression in a concise form using the definition of V_T as follows:

$$n_{2\text{-}DEG} = \frac{m_{||}^*}{\pi\hbar^2}\cdot kT\cdot exp\left[\frac{-h^2}{kT\cdot 8m_{||de}^*\cdot\left[t_{ch}+\frac{2}{\sqrt{2\cdot\Delta E_c}}\right]^2}\right]$$
$$\cdot exp\left\{\frac{q}{kT}(V_{GS}-V_T)\right\} \tag{7}$$

The areal channel charge density (Q_{ch}) can be obtained by multiplying the $n_{2\text{-}DEG}$ with the electron charge (q) while the gate capacitance per unit area (C_g) can be defined by the derivative of Q_{ch} with V_{GS}, yielding the following expressions:

$$|Q_{ch}| = q\cdot\frac{m_{||}^*}{\pi\hbar^2}\cdot kT\cdot exp\left[\frac{-h^2}{kT\cdot 8m_{||}^*\cdot\left[t_{ch}+\frac{2}{\sqrt{2\cdot\Delta E_c}}\right]^2}\right]$$
$$\cdot exp\left\{\frac{q}{kT}(V_{GS}-V_T)\right\} \tag{8}$$

$$C_g \triangleq \frac{\partial|Q_{ch}|}{\partial V_{GS}}$$
$$= q\cdot\frac{m_{||}^*}{\pi\hbar^2}\cdot kT\cdot exp\left[\frac{-h^2}{kT\cdot 8m_{||}^*\cdot\left[t_{ch}+\frac{2}{\sqrt{2\cdot\Delta E_c}}\right]^2}\right]$$
$$\frac{q}{kT}\cdot exp\left\{\frac{q}{kT}(V_{GS}-V_T)\right\} \tag{9}$$

We can rewrite Eq. (8) in a concise form using the definition of C_{gT}, which is the gate capacitance at threshold:

$$|Q_{ch}| = \frac{kT}{q}\cdot C_{gT}\cdot exp\left\{\frac{q}{kT}(V_{GS}-V_T)\right\} \tag{10}$$

We further define

$$C_{gT} \triangleq C_g(V_{GS}=V_T) = \frac{q^2\cdot m_{||}^*}{\pi\hbar^2}$$
$$\cdot exp\left[\frac{-h^2}{kT\cdot 8m_{||}^*\cdot\left[t_{ch}+\frac{2}{\sqrt{2\cdot\Delta E_c}}\right]^2}\right]. \tag{11}$$

(b) Inversion regime: The detailed view of the electrostatics of the In$_x$Ga$_{1-x}$As/In$_{0.52}$Al$_{0.48}$As QW MISFET in the inversion regime is shown in Fig. 4. In fact, for $V_{GS} > V_T$, the electrostatics of the device are profoundly affected by the presence of $n_{2\text{-}DEG}$. Applying a gate voltage that exceeds V_T requires an increase in the magnitude of the charge dipole across the metal–insulator–semiconductor (MIS) structure, where In$_{0.52}$Al$_{0.48}$As acts as the insulator and In$_x$Ga$_{1-x}$As
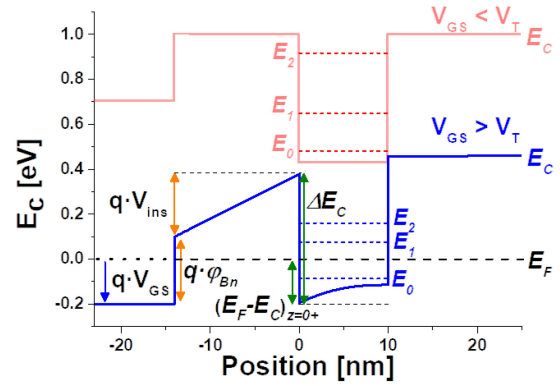
FIGURE 4. E_C of the In$_x$Ga$_{1-x}$As/In$_{0.52}$Al$_{0.48}$As QW FET during the inversion regime.

acts as the semiconductor. This leads to the band bending of E_C for both the In$_{0.52}$Al$_{0.48}$As insulator and In$_x$Ga$_{1-x}$As channel regions, as shown in Fig. 4. Since there is no volume charge density in the In$_{0.52}$Al$_{0.48}$As insulator, its band bending becomes linear with the z axis, whereas the band bending of the In$_x$Ga$_{1-x}$As channel becomes parabolic owing to the presence of $n_{2\text{-}DEG}$.

Since the DOS is finite in a semiconductor QW, the Fermi–level needs to increase above the conduction band edge as the channel charge density in the QW increases. This movement of the Fermi-level requires energy, causing a reduction of the inversion-layer capacitance (C_{inv}) [30]. This is the so–called DOS bottleneck, which becomes critical in Section III-V materials with the small electron's effective mass. By examining Fig. 4, we obtain

$$q\cdot\varphi_{Bn}+q\cdot V_{ins}=q\cdot V_{GS}+\left\{\Delta E_c-(E_F-E_c)_{z=0^+}\right\} \tag{12}$$

where V_{ins} is the voltage drop across the In$_{0.52}$Al$_{0.48}$As insulator, and $(E_F-E_c)_{z=0^+}$ indicates the amount of penetration of E_F in E_c on the surface of the In$_x$Ga$_{1-x}$As QW channel. Solving for V_{ins}, we get

$$V_{ins}=V_{GS}-\varphi_{Bn}+\frac{\Delta E_c}{q}-\frac{(E_F-E_C)_{z=0^+}}{q} \tag{13}$$

From the *sheet–charge approximation* (SCA), the amount of Q_{ch} can be given by the product of the areal insulator capacitance (C_{ins}) and V_{ins}. This yields

$$|Q_{ch}|=C_{ins}\times V_{ins} \tag{14}$$

By plugging Eq. (13) into Eq. (14), we finally obtain

$$|Q_{ch}|=C_{ins}\times\left[V_{GS}-\left(\varphi_{Bn}-\frac{\Delta E_c}{q}+\frac{(E_F-E_C)_{z=0^+}}{q}\right)\right] \tag{15}$$

Unlike Si MOS structures, $(E_F-E_c)_{z=0^+}$ in the inversion regime for the In$_x$Ga$_{1-x}$As QW structure continues to increase with V_{GS}, mainly owing to the DOS bottleneck in In$_x$Ga$_{1-x}$As. In an effort to approximate the behavior of $(E_F-E_c)_{z=0^+}$ with respect to V_{GS}, we investigated the numerical solution using a 1D *Poisson–Schrödinger* solver
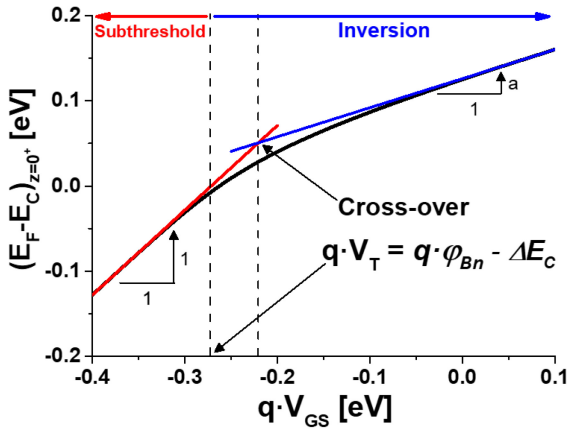
FIGURE 5. $(E_F - E_c)_{z=0^+}$ on the surface of the $In_{0.7}Ga_{0.3}As$ QW channel as a function of V_{GS}.

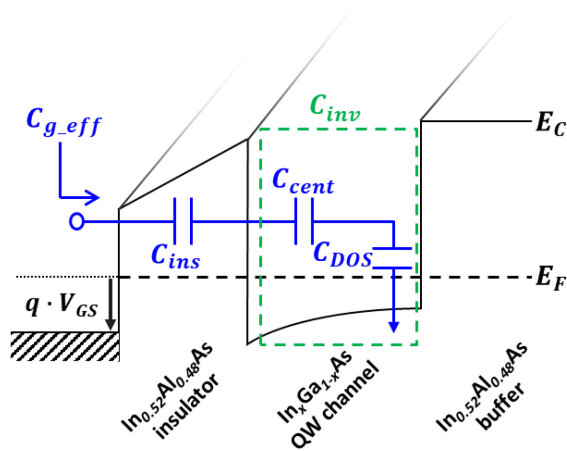**FIGURE 6.** Equivalent circuit model for the effective gate capacitance (C_{g_eff}) of an $In_xGa_{1-x}As/In_{0.52}Al_{0.48}As$ QW FET in the strong inversion regime.

from the Next-Nano simulator. Figure 5 plots $(E_F - E_c)_{z=0^+}$ as a function of $q.V_{GS}$, as obtained from the 1D simulation for the same structure shown in Fig. 1 (b). As expected, $(E_F - E_c)_{z=0^+}$ increases linearly with $q.V_{GS}$ with a slope of unity for $V_{GS} < V_T$ (subthreshold). Interestingly, $(E_F - E_c)_{z=0^+}$ continues to increase and eventually becomes linear with a slope of less than unity for $V_{GS} > V_T$. By approximating $(E_F - E_c)_{z=0^+}$ as $q.(a \times V_{GS} + b)$ in the strong inversion regime, Eq. (15) can be rewritten as follows:

$$|Q_{ch}| = (1-a) \cdot C_{ins} \cdot \left[V_{GS} - \frac{V_T + b}{1-a} \right] \quad (16)$$

Note that Eq. (15) is valid only for $V_{GS} \gg V_T$, which is in the strong inversion regime.

Next, let us think about the physical meanings of a and b. The effective gate capacitance, C_{g_eff}, of the $In_xGa_{1-x}As$ QW MISFET in the strong inversion regime can be modeled as a series combination of the insulator capacitance (C_{ins}) and inversion-layer capacitance (C_{inv}), as shown in Fig. 6, [30].

Then, C_{inv} consists of the DOS capacitance, C_{DOS} (frequently, it is also called the quantum capacitance, C_Q), and centroid capacitance, C_{cent}, owing to the QM distribution of n_o in the $In_xGa_{1-x}As$ QW [30]. From the charge–voltage relation of Eq. (16), C_{g_eff} is equal to $(1-a).C_{ins}$. By solving for a, we obtain

$$a = 1 - \left[1 + \frac{C_{ins}}{C_{inv}} \right]^{-1} \quad (17)$$

It is important to note that a is less than unity and thus reveals the degree of reduction of C_{g_eff} from C_{ins} due to the DOS bottleneck and QM effects. As will be discussed in the following section, we obtain a value of $a = 0.34$ for the $In_{0.7}Ga_{0.3}As/In_{0.52}Al_{0.48}As$ QW structure, revealing that we benefit only 66% from the insulator capacitance in the strong inversion regime.

From the energy band diagram in the subthreshold regime, V_T was defined such that $E_C(z = 0^+)$ touched E_F, as in Eq. (1) above. As indicated in Fig. 5, let us consider the physical meaning of the cross–over voltage between the two lines. This is exactly the threshold voltage in the strong inversion regime, as will be clear subsequently. Let us define this cross–over voltage as V_{T_inv}. Mathematically, V_{T_inv} can be formulated by equating the two lines and can be expressed as follows:

$$V_{T\_inv} = \frac{V_T + b}{1-a} \quad (18)$$

Note that Eq. (18) is exactly the *x*-intercept of Eq. (16), which is the threshold voltage in the strong inversion regime. As a result, b indicates the amount of shift of the threshold voltage defined in the subthreshold regime, and this V_{T_inv} is exactly what determines the areal channel charge density in the strong inversion regime, together with C_{g_eff}.

(c) Near-threshold regime: We are now in a position to develop a unified and continuous expression for the areal channel charge density from the subthreshold to strong inversion regimes. To do so, we investigated the most widely used expression for virtual-source models, which was first proposed by Khakifirooz *et al.* [17] and later revised by Rakheja *et al.* [18]. According to the pioneering work by Wright [31], the basic form of the expression for Q_{ch} is given as follows:

$$Q_{ch} = -C_{g\_eff} \cdot \frac{kT}{q} \cdot ln\left\{ 1 + exp\left(\frac{V_{GS} - V_T}{kT/q} \right) \right\} \quad (19)$$

Here, it is important to recognize that the threshold voltage to describe Q_{ch} in the subthreshold regime should be different from that in the strong inversion regime, as discussed in the previous two sub–sections. As a result, two different values of V_T have to be considered in Eq. (19) to fully describe Q_{ch} from the subthreshold to strong inversion regimes. It was found empirically in [17] that a shift of V_T by $3.5 \times kT/q$ was a very good approximation in advanced Si FETs. In this work, we revised the form of the "inversion-layer transition" function, F_f, such that the shape of the

TABLE 1. List of the seven physical and geometrical parameters, along with three transition coefficients. Other computed key parameters, such as V_T, V_{T_inv}, C_{gT} and C_{g_eff}, are included.

$q \cdot \varphi_{BN}$ [eV]	ΔE_C [eV]	t_{ch} [nm]	t_{ins} [nm]	ε_{r_ch}	ε_{r_ins}	$m_{\parallel}^*$ [eV·s²·cm⁻²]	α	β	η	V_T [V]	V_{T_inv} [V]	C_{gT} [µF/cm²]	C_{g_eff} [µF/cm²]
0.3	0.572	10	14	13.9	12.47	2.07×10^{-17}	0.7	2.6	1.0	-0.272	-0.221	0.27	0.52

threshold voltage transition was accurately captured with two transition parameters of α and β. In essence, this originates from the *Fermi–Dirac distribution function*, which allows smooth transition between the two different values of V_T as follows:

$$F_f(V_{GS}) = \cfrac{1}{1 + exp\left\{\cfrac{V_{GS} - \left(\frac{V_T + V_{T\_inv}}{\beta}\right)}{\alpha \cdot (q/kT)}\right\}} \quad (20)$$

Three key properties must be noted about the inversion-layer transition function: (i) at $V_{GS} = (V_T + V_{T\_inv})/\beta$, the function is exactly 1/2, (ii) $F_f(V_{GS})$ has a shape mirroring $1 - F_f(V_{GS})$ around $V_{GS} = (V_T + V_{T\_inv})/\beta$ and (iii) the transition of $F_f(V_{GS})$ from 1 to 0 around $(V_T + V_{T\_inv})/\beta$ gets sharper with decreasing α. Using the inversion-layer transition function, the unified Q_{ch} model from the subthreshold to strong inversion regimes can be expressed as follows:

$$Q_{ch} = -C_{g\_eff} \cdot \frac{kT}{q}$$
$$\cdot \, ln\left[1 + exp\left(\frac{V_{GS} - (V_{T\_inv} - \Delta V_T \cdot F_f)}{\frac{kT}{q}}\right)\right] \quad (21)$$

Here, ΔV_T is the difference between the two threshold voltages. In summary, the proposed Q_{ch} model in this work requires seven physical and geometrical parameters: the Schottky barrier height ($q \cdot \varphi_{BN}$), conduction-band discontinuity (ΔE_C), in-plane effective mass of the QW channel layer ($m_{\parallel}^*$), channel–layer thickness (t_{ch}), insulator–layer thickness (t_{ins}), permittivity of the channel layer (ε_{r_ch}), and permittivity of the insulator layer (ε_{r_ins}). The model also contains three transition coefficients (α, β, and η): α controls the sharpness of the transition between the subthreshold and inversion regimes, β determines the value of V_{GS} for the intermediate value halfway in the transition function, and η is the ideality factor that controls the sharpness of the subthreshold characteristics for $V_{GS} < V_T$ and enables to describe the dependency of the channel charge density on L_g.

III. RESULTS AND DISCUSSION

In the previous section, we presented the construction of the unified Q_{ch} model for $In_xGa_{1-x}As/In_{0.52}Al_{0.48}As$ QW MISFETs, which included the DOS bottleneck and QM effects, and was capable of describing its behaviors from the subthreshold to strong inversion regimes. In this section, we first verify suitability of the proposed model by comparison with the results obtained from the 1D *Poisson–Schrödinger* Solver. Then, we check the extension ability of our proposed
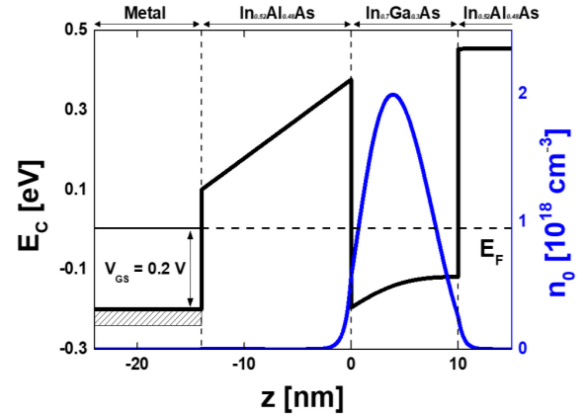
FIGURE 7. E_C (left) and n_o (right) profiles obtained from the 1D numerical simulator at $V_{GS} = 0.2$ V.

model by comparing its 1st-, 2nd- and 3rd-order derivatives. Next, we compare the experimental gate capacitance of fabricated $In_{0.7}Ga_{0.3}As$ MISFETs with the predictions of the gate capacitance derived by differentiating the modeled Q_{ch} with respect to V_{GS}. From this, we verify the validity of the proposed Q_{ch} model for the $In_xGa_{1-x}As/In_{0.52}Al_{0.48}As$ QW MISFETs.

The 1D simulation structure is identical to that shown in Fig. 1 (b) and consists of a gate metal stack of Pt/Ti/Pt/Au, 11–nm thick $In_{0.52}Al_{0.48}As$ insulator, 10–nm thick $In_{0.7}Ga_{0.3}As$ channel layer, and 300–nm thick $In_{0.52}Al_{0.48}As$ buffer on a semi-insulating 3-inch InP substrate. This structure is a typical $In_{0.7}Ga_{0.3}As$ MISFET design that our research group has fabricated and reported on recently [25]. Table 1 lists the physical and geometrical parameters for the 1D simulation structure. Figure 7 shows the conduction band and electron concentration (n_o) profiles of the 1D structure with $V_{GS} = 0.2$ V. Since the Next-nano solver performs a self-consistent 1D solution of the *Poisson–Schrödinger* equation, it provides the ideal channel charge densities for different values of V_{GS}. Therefore, the predictions from the Next-nano solver are used to validate the physics–based analytical Q_{ch} model proposed in the previous section. As discussed in Section II, V_T in the proposed model is set by the difference between Schottky barrier height ($q \cdot \varphi_{BN}$) and conduction-band discontinuity (ΔE_C), which would be directly applicable to III-V MISFETs and MOSFETs. Moreover, the proposed model could also find its extensibility for III-V high-electron-mobility transistors (HEMTs) and GaN FETs with a minor modification of
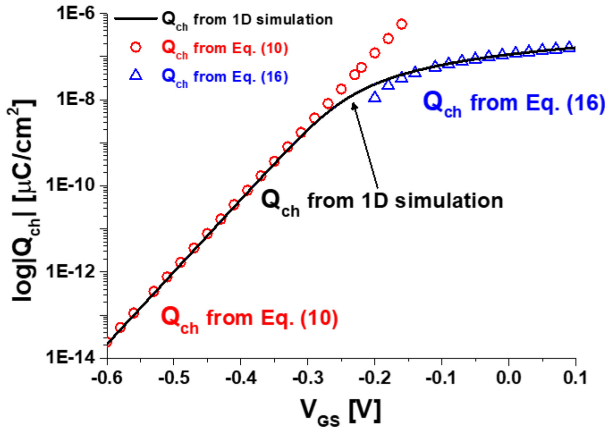
FIGURE 8. Semi-log plot of $|Q_{ch}|$ against V_{GS}. The modeled ones come from Eq. (10) for subthreshold and Eq. (16) for inversion, where the 1D simulation result is included for comparison.

FIGURE 9. Semi-log plot of $|Q_{ch}|$ against V_{GS} (on the left y-axis) and $|Q_{ch}|$ against V_{GS} (on the right y-axis). The modeled results come from Eq. (19) with two different values of the threshold voltage.

the threshold condition, taking the modulation-doping and piezoelectric effects into account.

Figure 8 plots the areal channel charge density of the In$_{0.7}$Ga$_{0.3}$As MISFET 1D structure on the logarithmic scale as a function of V_{GS}. The solid line is the numerical simulation result that is derived directly from the Next-nano solver, and the two types of symbols correspond to the results from our analytical expressions for Q_{ch} in the subthreshold (circles) and inversion (triangles) regimes, respectively. The key parameters, such as V_T, V_{T_inv}, C_{gT}, and C_{g_eff}, which are used to calculate Q_{ch} from Eqs. (10) and (16), are also included in Table 1. Note that the proposed analytical equations of Eqs. (10) and (16) are capable of describing Q_{ch} in both the subthreshold and inversion regimes. Figure 9 compares the modeled Q_{ch} from Eq. (18), which requires only one value of V_T, with the 1D numerically simulated Q_{ch}, in both the logarithmic (left y-axis) and linear (right y-axis) scales. The choices of the line and symbol type are identical to that in Fig. 8. Clearly, it is impossible to describe Q_{ch} from Eq. (18) with a single value of V_T, thereby demanding dual values of V_T as well as use of the inversion-layer transition function between the subthreshold and strong inversion regimes.

The findings in Fig. 9 motivated us to investigate use of the inversion-layer transition function in detail. Figures 10 (a) and (b) show the shapes of the inversion-layer transition function for (a) various values of α with a fixed value of β and (b) various values of β with a fixed value of α. As expected, α controls the sharpness of the transition between the subthreshold and inversion regimes, and the lower the value of α, the sharper is the transition of the inversion–layer transition function. β determines the value of V_{GS} such that the inversion–layer transition function is halved. The lower the value of β, the more negative the shift of the inversion–layer transition function, which is toward the threshold voltage defined in the subthreshold regime. Figure 11 (a) compares the modeled Q_{ch} obtained from
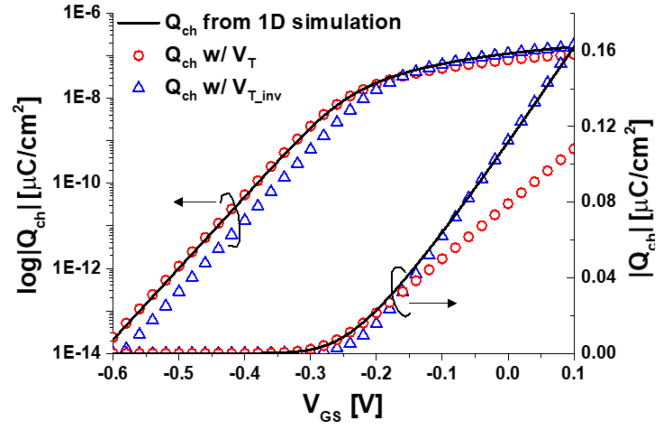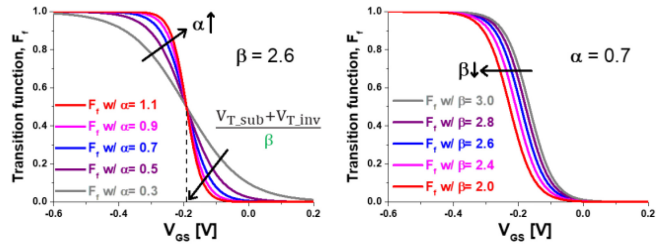

FIGURE 10. Inversion-layer transition function (F_f) against V_{GS}: (a) for various values of α with a fixed value of $\beta = 2.6$ and (b) for various values of β with a fixed value of $\alpha = 0.7$.
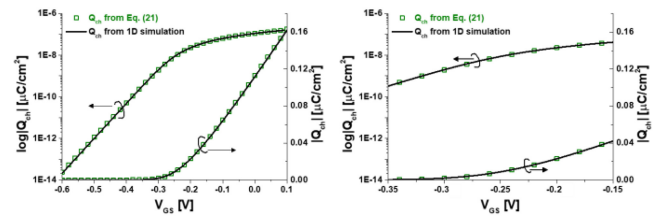

FIGURE 11. (a) Semi-log plot of $|Q_{ch}|$ against V_{GS} (on the left y-axis) and $|Q_{ch}|$ against V_{GS} (on the right y-axis), and (b) magnified plot.

Eq. (21) for various combinations of α and β with the 1D numerically simulated Q_{ch} in both the logarithmic (left y-axis) and linear (right y-axis) scales. Since it was assumed that there was no interfacial state density at the interface between the In$_{0.52}$Al$_{0.48}$As insulator and In$_{0.7}$Ga$_{0.3}$As channel layers in the 1D numerical simulation, the value of the ideality factor was chosen to be unity. A combination of $\alpha = 0.7$ and $\beta = 2.6$ yields the best explanation for Q_{ch} between the subthreshold and inversion regimes in the 1D structure studied in this work, as can be seen in the magnified plot of Fig. 11 (b).

To apply the proposed channel charge density model in future RF and mixed-signal systems, it is important to verify that the model provides accurate predictions of its higher-order derivatives, at least up to the 3rd-order derivative. Figures 12 (a), (b), (c) and (d), respectively,
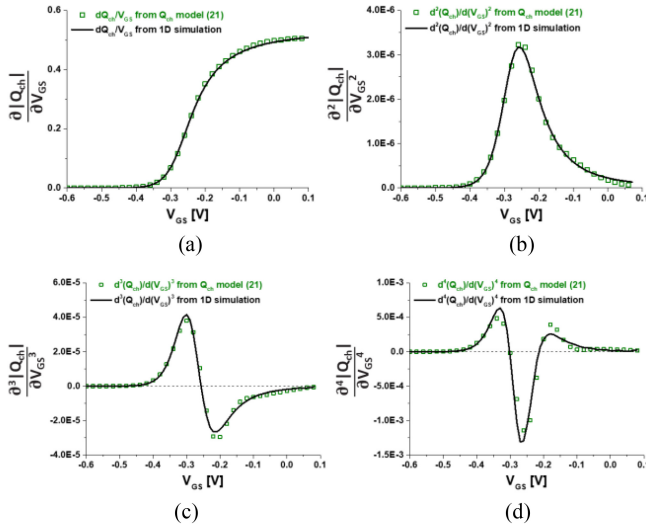
FIGURE 12. Comparison of higher-order derivatives of Q_{ch} with V_{GS}: (a) 1st-order derivative, (b) 2nd-order derivative, (c) 3rd-order derivative and (d) 4th-order derivative.

FIGURE 13. Comparison of the analytically modeled (this work) and 1D simulated Q_{ch} at different temperatures: (a) 200 K, (b) 100 K, (c) 77 K and (d) 4 K.

FIGURE 14. Comparison between the measured and projected subthreshold-swing (*S*) as a function of temperature.

show the comparison of 1st-order, 2nd-order, 3rd-order and 4th-order derivatives between the proposed charge model in this work and the 1D numerical simulation. Our model is capable of accurately describing the nature of all higher-order derivatives. To test the flexibility of our proposed charge model for low-temperature applications, we next investigate the accuracy of its prediction as temperature decreases. Figures 13 (a), (b), (c) and (d), respectively, compare the analytically modeled and 1D simulated Q_{ch} at 200 K, 100 K, 77 K and 4 K. Clearly, our model can capture the behavior of Q_{ch} at low temperatures without introducing any new parameters. Since the temperature-dependent subthreshold characteristics are explored, it will be interesting to see how the dependence of subthreshold-swing (*S*) in the modeled channel-charge characteristics on temperature could be correlated with the experimental one. Using the experimental report on temperature-dependent subthreshold characteristics of $L_g = 2$ μm $In_{0.7}Ga_{0.3}As$ HEMT, we compared the measured values of *S* from the I-V characteristics to the projected values of *S* from the channel charge model as a function of temperature, as shown in Fig. 14. Note that the model is fully capable of nicely projecting the temperature-dependent subthreshold-swing characteristics down to 77 K.

Next, we compare the prediction of the gate capacitance ($C_{g\_modeled}$) with the experimental gate capacitance ($C_{g\_meausred}$) for the fabricated $In_{0.7}Ga_{0.3}As$ MISFETs reported previously [25]. Here, $C_{g\_modeled}$ was obtained by differentiating the modeled Q_{ch} from Eq. (21) with V_{GS}, and $C_{g\_measured}$ was from 1 MHz capacitance–voltage (CV) measurements for the fabricated long-L_g devices. Figure 15 compares $C_{g\_modeled}$ with $C_{g\_measured}$. The total gate capacitance predicted from the model (red line) is seen to be in excellent agreement with the measured values (blue
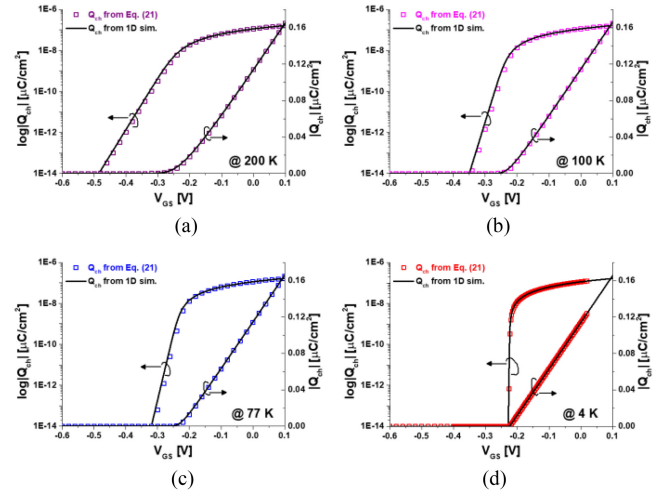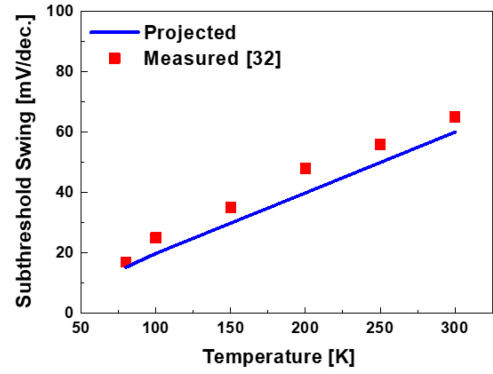
squares). This result increases the credibility of the calculation of the areal channel charge density from the proposed analytical expression using only 10 parameters (seven physical/geometrical parameters and three transition coefficients).

Finally, we attempt to verify our channel charge model by constructing a charge-based model for the I-V characteristics of $In_xGa_{1-x}As/In_{0.52}Al_{0.48}As$ QW FETs and comparing them with the experimental results [25], where the MIT virtual-source (MVS) model is considered for this purpose [33]–[34]. This is a simple semi-empirical model originally developed for short-L_g Si and III-V devices that is continuous from weak to strong inversion and from the linear to saturation regimes of operation. Figures 16 compares the predictions of the MVS model with measured I-V characteristics of the same $In_{0.7}Ga_{0.3}As$ MISFETs with $L_g = 2$ μm [25]. Excellent agreement is achieved with a combination of effective mobility (ε_{eff}) of 12,000 cm^2/V·s and injection velocity (v_{ox}) of 4.7×10^7 cm/s, increasing the credibility of our channel charge modeling process.
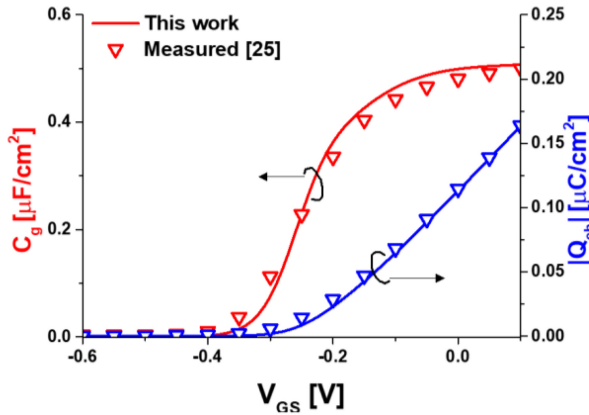
FIGURE 15. Comparison of the measured and modeled C_g against V_{GS} on the left *y*-axis and $|Q_{ch}|$ against V_{GS} on the right *y*-axis.
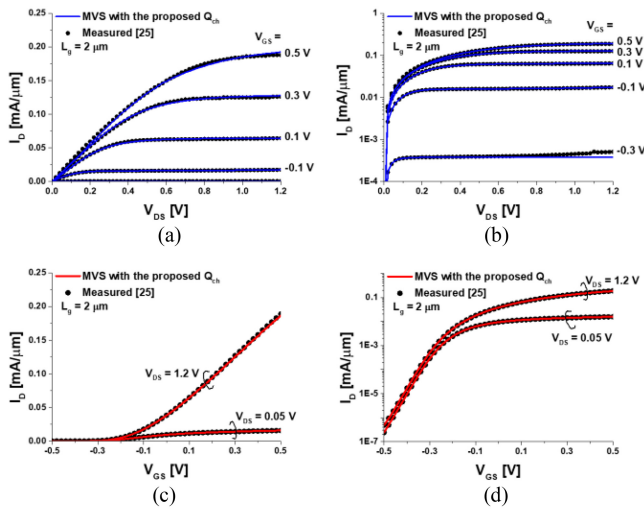

FIGURE 16. Comparison between the measured and MVS modeled I-V characteristics for the $L_g = 2$ μm In$_{0.7}$Ga$_{0.3}$As MISFET [25].

IV. CONCLUSION

This paper presented a comprehensive physics–based analytical channel charge model for indium-rich In$_x$Ga$_{1-x}$As/In$_{0.52}$Al$_{0.48}$As QW FETs that was applicable from the subthreshold to strong inversion regimes. The model required only seven physical/geometrical parameters and three transition coefficients. Since it was sufficient to consider only the 1st energy level (E_0) occupation in both the subthreshold and strong inversion regimes, the dependency of energy separation between E_F and E_C on the surface of the In$_x$Ga$_{1-x}$As QW channel for V_{GS} enabled construction of the charge–voltage behaviors of the In$_x$Ga$_{1-x}$As/In$_{0.52}$Al$_{0.48}$As QW 1D structure in each regime. To combine Q_{ch} between the subthreshold and strong inversion regimes, we revisited the previously proposed formula for the inversion-layer transition function, wherein we revised the function with three transition coefficients of α, β, and η. The proposed physics–based analytical Q_{ch} model yielded excellent agreement with the fabricated In$_{0.7}$Ga$_{0.3}$As/In$_{0.52}$Al$_{0.48}$As MISFETs and is

expected to be directly applicable to compact modeling of these devices.

REFERENCES

[1] J. A. del Alamo, "Nanometre-scale electronics with III–V compound semiconductors," *Nature*, vol. 479, pp. 317–323, Nov. 2011.
[2] J. Wang and M. Lundstrom, "Ballistic transport in high electron mobility transistors," *IEEE Trans. Electron Devices*, vol. 50, no. 7, pp. 1604–1609, Jul. 2003.
[3] D.-H. Kim, J. A. del Alamo, D. A. Antoniadis, and B. Brar, "Extraction of virtual-source injection velocity in sub-100 nm III–V HFETs," in *Proc. IEEE Int. Electron Devices Meeting (IEDM)*, 2009, pp. 1–4.
[4] N. Kharche, G. Klimeck, D.-H. Kim, J. A. del Alamo, and M. Luisier, "Performance analysis of ultra-scaled InAs HEMTs," in *Proc. IEEE Int. Electron Devices Meeting (IEDM)*, 2009, pp. 1–4.
[5] G. Dewey *et al.*, "Carrier transport in high-mobility III–V quantum-well transistors and performance impact for high-speed low-power logic applications," *IEEE Electron Device Lett.*, vol. 29, no. 10, pp. 1094–1097, Oct. 2008.
[6] C. M. Cooke *et al.*, "A 670 GHz integrated InP HEMT direct-detection receiver for the tropospheric water and cloud ice instrument," *IEEE Trans. THz Sci. Technol.*, vol. 11, no. 5, pp. 566–576, Sep. 2021.
[7] H. Hamada *et al.*, "Millimeter-wave InP device technologies for ultra-high speed wireless communications toward beyond 5G," in *Proc. IEEE Int. Electron Devices Meeting (IEDM)*, 2019, pp. 1–4.
[8] M. Kotiranta *et al.*, "Cryogenic 50-nm mHEMT MMIC LNA for 67-116 GHz with 34 K noise temperature," in *Proc. Global Symp. Millimeter Waves (GSMM) ESA Workshop Millimetre Wave Technol. Appl.*, 2016, pp. 1–3.
[9] C. B. Zota *et al.*, "III-V-on-CMOS devices and circuits: Opportunities in quantum infrastructure," in *Proc. IEEE Int. Electron Devices Meeting (IEDM)*, 2019, pp. 1–4.
[10] E. Cha, N. Wadefalk, G. Moschetti, A. Pourkabirian, J. Stenarson, and J. Grahn, "A 300-μW cryogenic HEMT LNA for quantum computing," in *IEEE/MTT-S Int. Microw. Symp. Dig.*, 2020, pp. 1299–1130.
[11] E. Cha, N. Wadefalk, G. Moschetti, A. Pourkabirian, J. Stenarson, and J. Grahn, "InP HEMTs for sub-mW cryogenic low-noise amplifiers," *IEEE Electron Device Lett.*, vol. 41, no. 7, pp. 1005–1008, Jul. 2020.
[12] D. Delagebeaudeuf and N. T. Linh, "Metal-(n) AlGaAs-GaAs two-dimensional electron gas FET," *IEEE Trans. Electron Devices*, vol. TED-29, no. 6, pp. 955–960, Jun. 1982.
[13] U. Radhakrishna, P. Choi, and D. A. Antoniadis, "Facilitation of GaN-based RF- and HV-circuit designs using MVS-GaN HEMT compact model," *IEEE Trans. Electron Devices*, vol. 66, no. 1, pp. 95–105, Jan. 2019.
[14] S. Khandelwal *et al.*, "ASM GaN: Industry standard model for GaN RF and power devices—Part 1: DC, CV, and RF model," *IEEE Trans. Electron Devices*, vol. 66, no. 1, pp. 80–86, Jan. 2019.
[15] I. Angelov, H. Zirath, and N. Rorsman, "A new empirical nonlinear model for HEMT and MESFET devices," *IEEE Trans. Microw. Theory Techn.*, vol. 40, no. 12, pp. 2258–2266, Dec. 1992.
[16] *ICCAP Software Documentation*, Agilent Technol. Inc., Palo Alto, CA, USA, 2009.
[17] A. Khakifirooz, O. M. Nayfeh, and D. Antoniadis, "A simple semiempirical short-channel MOSFET current–voltage model continuous across all regions of operation and employing only physical parameters," *IEEE Trans. Electron Devices*, vol. 56, no. 8, pp. 1674–1680, Aug. 2009.
[18] S. Rakheja, M. S. Lundstrom, and D. A. Antoniadis, "An improved virtual-source-based transport model for quasi-ballistic transistors—Part I: Capturing effects of carrier degeneracy, drain-bias dependence of gate capacitance, and nonlinear channel-access resistance," *IEEE Trans. Electron Devices*, vol. 62, no. 9, pp. 2786–2793, Sep. 2015.
[19] L. Wei, O. Mysore, and D. Antoniadis, "Virtual-source-based self-consistent current and charge FET models: From ballistic to drift-diffusion velocity-saturation operation," *IEEE Trans. Electron Devices*, vol. 59, no. 5, pp. 1263–1271, May 2012.
[20] X. Cheng and Y. Wang, "A surface-potential-based compact model for AlGaN/GaN MODFETs," *IEEE Trans. Electron Devices*, vol. 58, no. 2, pp. 448–454, Feb. 2011.
[21] S. Emekar *et al.*, "Modified Angelov model for an exploratory GaN-HEMT technology with short, few-fingered gates," in *Proc. Int. Conf. Simul. Semicond. Process. Devices (SISPAD)*, 2017, pp. 117–120.

[22] Y. H. Chang and J. J. Chang, "Analysis of an EEHEMT model for InP pHEMTs," in *Proc. Conf. Electron Devices Solid-State Circuits*, 2007, pp. 237–240.

[23] W. R. Curtice and M. Ettenberg, "A nonlinear GaAs FET model for use in the design of output circuits for power amplifiers," *IEEE Trans. Microw. Theory Techn.*, vol. TMTT-33, no. 12, pp. 1383–1394, Dec. 1985.

[24] T. Li, W. Li, and J. Liu, "An improved large signal model of InP HEMTs," *J. Semicond*, vol. 39, no. 5, 2018, Art. no. 54003.

[25] I.-G. Lee *et al.*, "Long-channel InAlAs/InGaAs/InAlAs single-quantum-well MISFETs with subthreshold swing of 61 mV/decade and effective mobility of 11,900 cm^2 V$^{-1}\cdots^{-1}$," *Appl. Phys. Exp.*, vol. 12, May 2019, Art. no. 64003.

[26] E.-Y. Chang, C.-I. Kuo, H.-T. Hsu, C.-Y. Chiang, and Y. Miyamoto, "InAs thin-channel high-electron-mobility transistors with very high current-gain cutoff frequency for emerging submillimeter-wave applications," *Appl. Phys. Exp.*, vol. 6, no. 3, Mar. 2013, Art. no. 34001.

[27] A. Leuther *et al.*, "20 nm metamorphic HEMT with 660 Ghz f$_T$," in *Proc. 23rd Int. Conf. Indium Phosph. Rel. Mater. (IPRM)*, Berlin, Germany, May 2011, pp. 1–4.

[28] X. Mei *et al.*, "First demonstration of amplification at 1 THz using 25-nm InP high electron mobility transistor process," *IEEE Electron Device Lett.*, vol. 36, no. 4, pp. 327–329, Apr. 2015.

[29] H.-B. Jo *et al.*, "L$_g$ = 25 nm InGaAs/InAlAs high-electron mobility transistors with both f$_T$ and f$_{max}$ in excess of 700 GHz," *Appl. Phys. Exp.*, vol. 12, no. 5, May 2019, Art. no. 54006.

[30] D. Jin, D. Kim, T. Kim, and J. A. del Alamo, "Quantum capacitance in scaled down III–V FETs," in *Proc. IEEE Int. Electron Devices Meeting (IEDM)*, 2009, pp. 1–4.

[31] G. T. Wright, "Threshold modeling of MOSFETs for CAD of CMOS VLSI," *Electron. Lett.*, vol. 21, no. 6, pp. 223–224, Mar. 1985.

[32] S.-W. Son, J.-H. Park, J.-M. Baek, J.-S. Kim, D.-K. Kim, and D.-H. Kim, "Low-temperature characteristics of In$_{0.7}$Ga$_{0.3}$As PHEMTs," in *Proc. Lester Eastman Conf. (LEC)*, 2016, pp. 12–14.

[33] H. Luo and A. Huang, "An improved sub-threshold swing model for MIT virtual source GaN model," in *Proc. IEEE MTT-S Int. Wireless Symp. (IWS)*, 2018, pp. 1–4.

[34] H. Elgabra, B. Buonacorisi, C. Chen, J. Watt, J. Baugn, and L. Wei, "Virtual source based I-V model for cryogenic CMOS devices," in *Proc. Int. Symp. VLSI Technol. Syst. Appl. (VLSI-TSA)*, 2019, pp. 1–2.